

**Fundamental insights about interlayer cation migration in
Li-ion electrodes at high states of charge**

Journal:	<i>Journal of Materials Chemistry A</i>
Manuscript ID	TA-ART-04-2019-003460
Article Type:	Paper
Date Submitted by the Author:	02-Apr-2019
Complete List of Authors:	Vinkeviciute, Julija; University of California Santa Barbara, Materials Radin, Maxwell; University of California Santa Barbara, Materials Faenza, Nicholas; Rutgers University, Department of Materials Science and Engineering Amatucci, Glenn; Rutgers University, Department of Materials Science and Engineering Van der Ven, Anton; University of California Santa Barbara, Materials



Cite this: DOI: 10.1039/xxxxxxxxxx

Fundamental insights about interlayer cation migration in Li-ion electrodes at high states of charge[†]

Julija Vinckevičiūtė,^a Maxwell D. Radin,^a Nicholas V. Faenza,^b Glenn G. Amatucci,^b and Anton Van der Ven^{*a}Received Date
Accepted Date

DOI: 10.1039/xxxxxxxxxx

www.rsc.org/journalname

One approach to increasing the capacity of Li-ion batteries is to expand the usable voltage range over which the battery is cycled by charging the cathode to higher voltages. Layered intercalation compounds commonly used as cathodes in Li-ion batteries, however, can become susceptible to irreversible structural changes at high states of charge due to cation migration to the emptied Li layers. Here we report on the discovery of a strong correlation between the position of the Fermi level and the energy barrier for cation migration to the Li layers of fully charged layered intercalation compounds. Since the identity of the transition metal strongly influences the Fermi level, this discovery suggests that cation migration can be suppressed at high states of charge using targeted alloying strategies. First-principles calculations indicate that an increase in the concentration of Ni relative to Co or Mn should reduce, or even impede, interlayer migration in layered oxides. The insights of this study pave the way for the discovery of layered intercalation compounds that can approach their theoretical capacities in practice.

1 Introduction

Layered LiCoO₂ was first introduced as a cathode material for Li-ion batteries in 1991,^{1,2} and its derivatives remain the current standard in many applications. This is in spite of their practical reversible capacity being limited to 50-70% of their total theoretical capacity.³ Capacities are in part limited due to structural changes that occur at high states of charge where the Li concentration of the host becomes very low.⁴ Strategies that suppress these irreversible changes are necessary to realize the full theoretical capacities of layered intercalation compounds, thereby enabling higher energy densities and lower costs.

One approach to improve on LiCoO₂ is to alloy the Co sublattice of the LiCoO₂ host with different transition metals (TM) or to dope it with non-redox active cations. For instance, NMC (Li_xNi_{1-y-z}Mn_yCo_zO₂) employs a mixture of TM elements (namely Ni, Mn, and Co) within the metal layers of the host,⁵ while NCA (Li_xNi_{1-y-z}Co_yAl_zO₂), combines a mixture of TM elements with a non-redox active dopant (i.e. Al).⁴ Not only does this tend to increase reversible capacity, but it also reduces cost by

utilizing more abundant elements.³ We refer to non-TM elements such as Al, Mg, or Li as dopants since their behavior within a layered intercalation compound differs from that of TM atoms in that they lack *d* orbitals for bonding and therefore are not expected to participate in redox upon (dis)charge.* The combination of transition metal alloying with non-transition metal doping has also led to new classes of materials that promise high capacities. This includes Li-rich materials, which while often having similar TM chemistries as NMC, also have an excess of Li that resides in the TM layers.⁶ Mg is also increasingly being investigated as a dopant in Na intercalation compounds.⁷

While significant improvements have been achieved through doping and alloying,^{3,8} very little is understood about the precise role that dopants play on battery performance. Some dopants such as Al⁹⁻¹² and Mg¹²⁻¹⁶ appear to suppress undesirable phase transitions when added to Li_xCoO₂, such as the O3 to O1 structural transition at high states of charge¹⁷⁻²¹ or the two-phase reaction due to the metal-insulator transition at high Li concentrations.²² Since the dopants are not redox active, they retain some Li ions within the host to maintain charge neutrality at high

^a Materials Department, University of California, Santa Barbara

^b Energy Storage Research Group, Department of Materials Science and Engineering, Rutgers University, North Brunswick

* Corresponding author. E-mail: avdv@ucsb.edu

[†] Electronic Supplementary Information (ESI) available. In addition, a publicly available database link with calculation files can be downloaded at: <http://dx.doi.org/doi:10.18126/M2Z7J>.

* Although non-transition metal dopants are added at much higher concentrations than the classical use of the word may imply, their concentrations in layered intercalation compounds are usually sufficiently low that they do not interact with each other in any appreciable way and can be viewed as dilute from an alloying perspective.

states of charge, thereby preventing a significant contraction of the c-lattice parameter.²¹ Layered electrode materials, however, are susceptible to irreversible structural changes at high states of charge due to the availability of many channels for interlayer cation migration that emerge when the Li-vacancy concentration is very high.^{8,14,23} These irreversible changes usually lead to an overall degradation of electrochemical properties. Thus, though dopants may prevent some structural transformations, they can also cause capacity loss via irreversible migration.

As an illustration of the effect of dopants on electrochemical properties, Figures 1(a) and (b) show the first charge and discharge voltage curves of Al doped Li_xNiO_2 and Li_xCoO_2 (i.e. $\text{Li}_x\text{Al}_y\text{Ni}_{1-y}\text{O}_2$ and $\text{Li}_x\text{Al}_y\text{Co}_{1-y}\text{O}_2$ for $y = 0, 0.05, 0.10$, and 0.2). This is a small subset of a large number of Co, Ni, and Co/Ni host materials synthesized, cycled, and characterized in Ref 21, where more details of synthesis conditions, particle size, and characterization can be found (see also experimental methods section). Electrode components and testing conditions were chosen to isolate irreversible capacity loss from kinetic factors and may not reflect commercial devices. The voltage window is sufficiently large (between 2.75 to 4.75 V) to ensure that the full theoretical capacity of each compound is accessed. As the concentration of Al increases, the initial charge capacity decreases since fewer redox-active TM atoms are available for oxidation at the end of charge. Dopants such as Al are viewed as beneficial because of their tendency to suppress detrimental structural phase transitions at high states of charge.^{9,11} This is evident in the voltage profiles of Figures 1(a) and (b), which show a smearing out of phase transition steps and plateaus even at low Al concentrations.

Close inspection of the voltage profiles of Figures 1(a) and (b) reveal a remarkable trend. While the initial capacity loss between first charge and discharge in the Ni compounds is large, it is relatively insensitive to Al concentration. The Co containing compounds, in contrast, exhibit a strong dependence of the first charge/discharge capacity loss on Al concentration. In fact, instead of reducing the first cycle capacity loss as expected, an increase in the Al concentration in Co hosts actually exacerbates it. This becomes clear when the capacity loss after the first cycle is plotted as a function of Al doping in the Ni and Co hosts as shown in Figure 1(c). The electrochemical data of Figure 1 shows not only that dopants can have a detrimental effect on capacity retention when a layered intercalation compound is charged to high voltages, but that its effect is also very sensitive to the host chemistry.

One possible explanation for the lost capacity after the first cycle is the irreversible migration of dopants out of the TM layer and into the Li layer. For instance, Al migration can block sites and prevent a portion of the Li from reintercalating upon discharge. In fact, NMR evidence suggests the presence of Al in the Li layers of the Co hosts after the first discharge.²¹ It is well known from studies of Li_xFePO_4 that TM-Li anti-site defects can have a strong effect on Li conductivity.^{24–27}

Here we describe the results of a first-principles electronic structure study that predicts a strong dependence of the driving force for dopant migration to the Li layer on host chemistry. We find that the energy of a dopant along the migration path from the

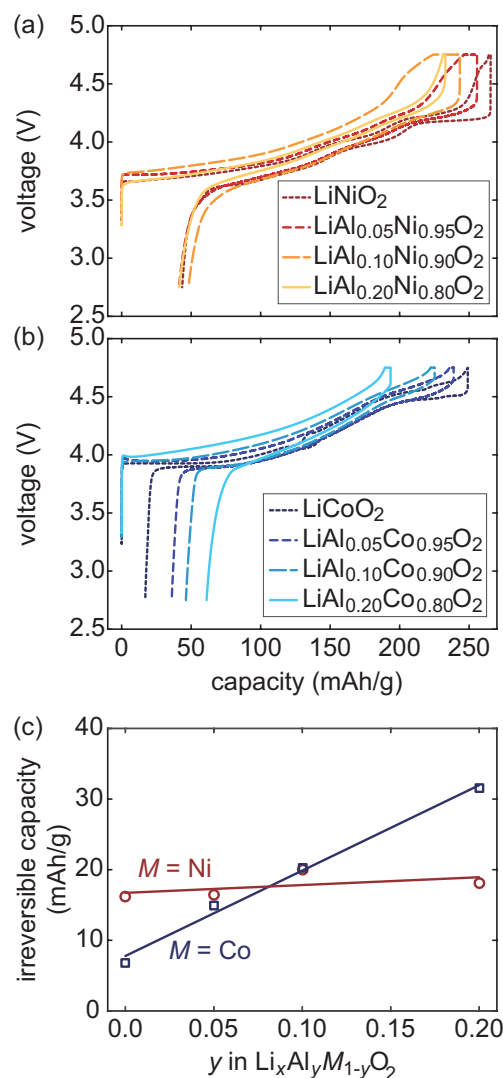


Fig. 1 Experimental cycling data of an Al dopant in (a) Ni host and (b) Co host with varying concentration of Al. (c) Comparing the first cycle irreversible capacity loss with increasing Al concentration in Ni and Co hosts (markers are data, lines are least-square linear fits).

transition metal layer to the Li layer is very sensitive to the position of the Fermi level. The susceptibility of dopants to migrate to the Li layer can, therefore, be controlled through modifications of the host chemistry, which determines the Fermi level. Our calculations predict that Ni-rich hosts will suppress dopant migration to the Li layer at high states of charge, while Co and Mn-rich hosts will not. Therefore, we expect Ni-rich hosts to experience smaller irreversible capacity losses upon cycling. Since many irreversible phase transitions that cause degradation require interlayer atom migration, understanding and suppressing this mechanism could increase reversible capacity and lengthen cathode lifetime. These insights suggest that important mechanisms of cathode degradation at high states of charge can be suppressed by alloying strategies that penalize dopant migration, thereby bringing us closer to realizing the full theoretical capacity of layered intercalation compounds.

2 Tendency of ions to migrate

To understand interlayer migration within the layered O3 crystal structure, we first describe a path that dopants likely follow as they move from the TM layer into the Li layer. The pristine synthesized material consists of transition-metal oxide (TM-O) sheets separated by filled, octahedrally coordinated Li. The dopant usually replaces about 5% of the TMs in the TM layer, as illustrated in Figure 2(a) with $\text{Li}_x\text{Mg}_y\text{Co}_{1-y}\text{O}_2$ ($x = 1$).^{3,12,14,16} In the fully lithiated state, cations in the TM layer cannot easily migrate to the Li layer since all of the octahedral Li sites are filled. However, upon charge, Li vacancies are introduced, allowing cations in the TM layer to hop into the emptying Li layer.^{8,14,23}

A cation in the TM layer must pass through an adjacent tetrahedral site before it can continue to an octahedral site of the Li layer. Figures 2(b)-(e) show a migration path by which the dopant can hop out of the TM layer and away from its original site; we use Mg migrating in a Co host as an example. In the fully charged state, there are two residual Li ions for every Mg dopant to maintain charge neutrality (assuming that Mg has a formal oxidation state of 2+ and the surrounding TM ions have a formal oxidation state of 4+). The dopant (D) is initially in an octahedral site in the TM layer (D_{Oct} configuration) (Figure 2(b)). Based on extensive density functional theory (DFT) calculations of the energies of different Li-vacancy orderings, we found that Li prefers to cluster around the dopant as illustrated in Figure 2(b) and (c). The vacancies in the Li layer, formed upon charging, open a pathway for the dopant to hop into an adjacent tetrahedral site in the Li layer. Figure 2 also shows the energies of structures (b)-(e) relative to the D_{Oct} configuration, as calculated with DFT. A low energy configuration that has Mg in the tetrahedral site is a Li-Mg dumbbell, D_{Tet} , as illustrated in Figure 2(c). While we have not calculated migration barriers, a reduction in energy of 500 meV when going from D_{Oct} to D_{Tet} (i.e. from Figure 2 (b) to (c)) constitutes a very large driving force for Mg migration out of the transition metal layer in the fully charged state. For migration between octahedral and tetrahedral sites, the hop barrier is dominated by the difference in energy between the two end states, with a considerably smaller contribution from intermediate positions, especially when the adjacent octahedral sites are vacant.²⁹⁻³³

If Li were re-intercalated into the structure when the dopant is in the D_{Tet} configuration, the dopant would likely return to the TM layer and the reversible migration would have little effect on material degradation.[†] However, if the dopant moves away from the vacancy in the TM layer, an energetically favorable Li-Li dumbbell will rapidly form³⁴ as illustrated in Figure 2 (d). Based on the Boltzmann distribution of the energy difference between configurations (c) and (d) at 300 K, Li-Li dumbbells would be about three orders of magnitude more probable than Li-Mg dumbbells. The stable Li-Li dumbbell is, therefore, likely to block the Mg from returning to its original site in the TM layer thereby keeping it in the Li layer. This scenario results in an irreversible structural change of the host that will affect capacity and the voltage profile of subsequent cycles.

The example of Figure 2 shows that Mg dopants in O3 Li_xCoO_2 experience a thermodynamic driving force to migrate to the Li layer towards the end of charge. Considering the irreversible and detrimental structural changes that such cation migration can inflict on the host, the question emerges: which other dopants and host chemistries exhibit a similar tendency for dopant migration to the Li layer in the fully charged state? Common dopants added to layered intercalation compounds include Al, Mg, and Li (the latter in Li-excess cathodes). Any cation that migrates to the Li layer will invariably form an intermediate Li-dopant dumbbell configuration, D_{Tet} , as illustrated in Figure 2(c).^{35,36} The difference in energy between the D_{Tet} configuration and the initial D_{Oct} state determines whether or not a dopant experiences a driving force to migrate to the Li layer at the end of charge. In the remainder, we focus on these two configurations.

Figure 3 compares the stability of the D_{Tet} configuration relative to D_{Oct} for Al, Mg, and Li dopants in the O3 forms of fully charged Ni, Co, and Mn hosts. The energies of many Li orderings were calculated for each system in the D_{Oct} and D_{Tet} configurations, and the lowest energy for each dopant configuration was used to calculate the energy differences of Figure 3. Negative energies indicate that the Li-dopant dumbbell is more stable and that the dopant therefore has a tendency to migrate to the Li layer. The formation energies become more negative as the oxidation state of the dopant decreases (i.e. $\text{Al}^{3+} \rightarrow \text{Mg}^{2+} \rightarrow \text{Li}^+$; moving down the chart for the same host). The lower the dopant's oxidation state, the more stable the D_{Tet} configuration becomes. More surprisingly, however, is the peculiar trend with respect to the host chemistry. The Co and Mn hosts exhibit similar energy differences for the same dopant and tend to prefer D_{Tet} configurations. The Ni host, in contrast, appears to penalize Li-dopant dumbbells. The implication of Figure 3 is that the Ni host will suppress dopant migration to the Li layer in the fully charged state since the crucial first step of the migration process results in an increase in energy. In the next sections, we explore the role that the electronic structure of the host plays in determining the susceptibility of dopant migration to the Li layer in these three hosts.

† If Mg did not return to the TM layer, the Li-Mg dumbbell would block some Li sites from reintercalation.

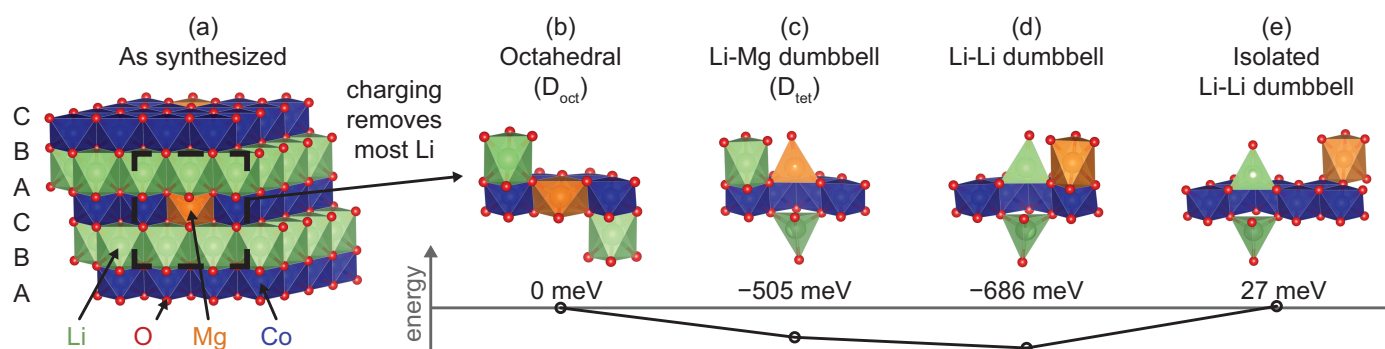


Fig. 2 Possible path for dopant to move out of the TM layer, into the Li layer, and away from the created vacancy upon delithiation; $\text{Li}_x\text{Mg}_y\text{Co}_{1-y}\text{O}_2$ ($x = 2y$) illustrated, with relative energies of each snapshot along the path indicated below each image. (a) Structure is synthesized with Mg in TM layer and filled Li layer. (b) Upon charge, Li is removed from the Li layer, resulting in the D_{oct} configuration. (c) Mg then migrates into the Li layer via Li-Mg dumbbell, eventually forming (d) a Li-Li dumbbell with an adjacent Mg. (e) Once the Li-Li dumbbell forms, a barrier exists for Mg to migrate away from the defect site. (Images made using VESTA²⁸)

3 Electronic structure in layered oxides

We first review the general understanding of the electronic structure of layered transition-metal oxides. Layered intercalation compounds consist of sheets of edge-sharing transition-metal oxide (TM-O) octahedra. A simplified molecular orbital diagram for σ bonding in an isolated TM-O octahedron (Figure 4(a)) already reveals important features about the electronic structure of layered intercalation compounds. The TM 3d, 4s, and 4p atomic orbitals hybridize with the O 2p orbitals to form bonding and anti-bonding molecular orbitals. The six lowest bonding levels have predominantly O p character. These are followed by three t_{2g} levels derived from the TM d_{xy} , d_{xz} , and d_{yz} orbitals that point between the O ions of the octahedron. While shown as non-bonding in Figure 4(a), the TM d_{xy} , d_{xz} , and d_{yz} orbitals in fact interact with O p orbitals to form π bonding and anti-bonding states with t_{2g} symmetry. The lowest anti-bonding orbitals have e_g symmetry (referred to as e_g^*) and are predominantly of $d_{z^2-x^2-y^2}$ and $d_{x^2-y^2}$ character.

The molecular orbital levels of Figure 4(a) become bands when the TM-O octahedra are brought together to form the periodic crystal structure of the layered intercalation compounds. This is shown for NiO_2 in Figure 4(b). The density of states (DOS) plot of Figure 4(c) exhibits three broad regions that coincide with the molecular orbital levels of the isolated TM-O octahedron. As is conventionally done, we will refer to these broad regions as corresponding to the O p , the t_{2g} , and the e_g states, respectively, as illustrated schematically in Figure 4(d). In NiO_2 , the Fermi level separating the filled from the unoccupied states falls between the t_{2g} and the e_g levels. In CoO_2 and MnO_2 , in contrast, the Fermi level resides within the t_{2g} block.

4 Transition metal substitution

In this section, we determine the effect of dopants having different oxidation states on the electronic structure of a fully delithiated transition-metal oxide. We replace one of the Ni atoms in a supercell of NiO_2 containing 16 primitive unit cells with either Al, Mg, Li, or a vacancy (Va). The choice of dopants is motivated not only by their technological importance, but also by the fact that

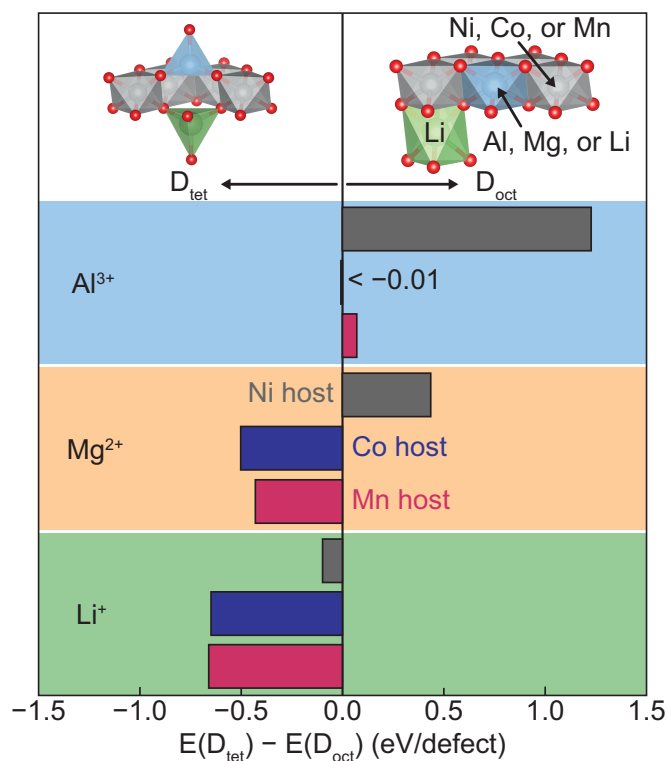


Fig. 3 Difference in energy between D_{oct} and D_{tet} configurations. Extra Li ions are added as necessary for charge compensation. Dumbbells are relatively more stable as dopant oxidation state decreases and more stable in Co and Mn hosts than in the Ni host. (Images made using VESTA²⁸)

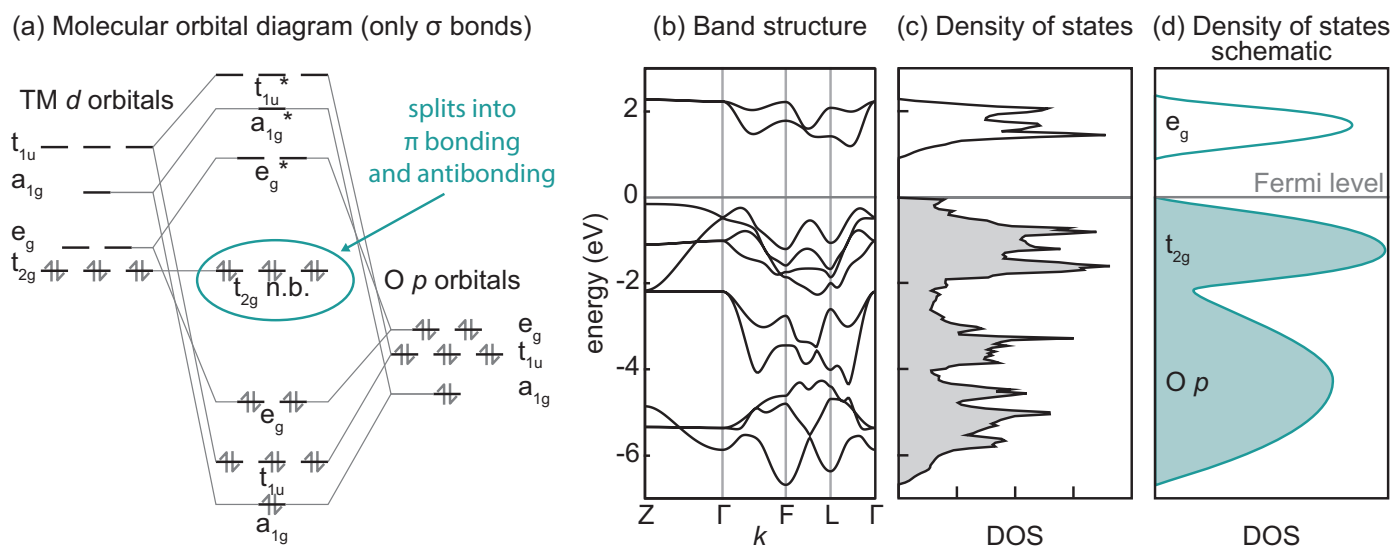


Fig. 4 Electronic structure of transition-metal layered oxides, using O3 NiO₂ as an example. (a) The molecular orbital diagram of an isolated Ni-O octahedron; only σ bonding is included in this simplified model. (b) The band structure for layered bulk NiO₂. (c) The sum of the bands at each energy level results in the density of states plot. (d) Schematic of the DOS, identifying the bands as mainly O p , t_{2g} , and e_g .

their formal oxidation state differs from each other and from that of the 4+ charge of the TM cations: i.e. Al³⁺, Mg²⁺, and Li⁺. We also consider a vacant TM site as a vacancy donates zero electrons to the host. By varying the dopant, we are effectively changing the local electrostatic potential experienced by the six O atoms adjacent to the defect. Since each dopant has a formal oxidation state that is lower than the 4+ oxidation of the transition metals, there must be residual Li ions in the Li layer to maintain charge neutrality in the fully charged state: one, two, three, and four Li must remain in the host for each Al, Mg, Li, and Va dopant, respectively. We will consider the explicit effect of these residual Li ions later. However, to qualitatively determine the effect of dopants on the electronic structure, we first perform calculations in the absence of explicit residual Li ions, instead adding their valence electrons to the host and compensating the excess negative charge with a uniform positive background charge.

The DOS for each dopant in NiO₂ are shown in Figure 5 and are aligned based on the bottom of the deep O s states (below the states shown in the figure). Though spin-polarized calculations were performed, the spin channels were identical and only one of them is shown. Localized peaks at the top of the t_{2g} and e_g blocks not present in the DOS of pure NiO₂ appear in the other four panels and are highlighted in red. We refer to these localized states as defect states because they form as a result of TM substitution by a vacancy or non-TM atom. All of the t_{2g} states are filled in NiO₂ and therefore significantly contribute to the overall energy unlike the defect states in the empty e_g block. Therefore, references to defect states in this work largely concern the localized t_{2g} states. Figure 5 clearly shows that as the oxidation state of the dopant decreases from left to right, the defect states become more prominent and increase in energy. Since the defect states are occupied in NiO₂, their rise also results in an increase in the Fermi level (relative to the deep O s states).

Figure 5 shows the electronic charge density associated

with the defect states when the dopant is a vacancy (i.e. Va_{1/16}Ni_{15/16}O₃₂). The figure is oriented looking down on a single layer of the TM oxide, and the yellow lobes are an isosurface of electron charge density. The majority contribution comes from the O and Ni atoms that immediately surround the vacancy. The high-energy defect states consist of six O p orbitals that point towards the vacancy and six Ni d orbitals that point between oxygen ions. The O p and Ni d orbitals are aligned for π bonding. The defect states for the other dopants exhibit similar electronic charge densities around the dopant site.

5 Dumbbell formation

Having determined that dopants generate high-energy defect states, we next consider the changes in electronic structure as the dopant migrates from the TM layer (D_{Oct} configuration) into a dumbbell (D_{Tet} configuration). In this section, we explicitly treat the residual Li ions that must remain in the Li layer to maintain charge neutrality in the fully charged state. For cases where multiple Li arrangements were possible, the lowest-energy configuration was used (of the ones calculated, details in ESI). In general, it was found that configurations that cluster Li around the defect have the lowest energy. We begin by considering dopants in the Ni host and then determine how the electronic structure changes when the same dopants were added to Co and Mn hosts.

Figure 6 compares the calculated DOS for NiO₂ with DOS for Li-Al in D_{Oct} and D_{Tet} configurations. Figure 6 (b) shows that the replacement of one octahedral Ni by Al results in defect states immediately below the Fermi level that are qualitatively similar to those around a vacancy as described in the previous section. One Li remains in the host for each Al dopant to maintain charge neutrality in the fully charged state. The lowest energy state has Li residing in an octahedron that shares a corner with the Al octahedron. Site projected DOS (figure in ESI) shows that the defect states comprise of O p and Ni d orbitals from O and Ni that neigh-

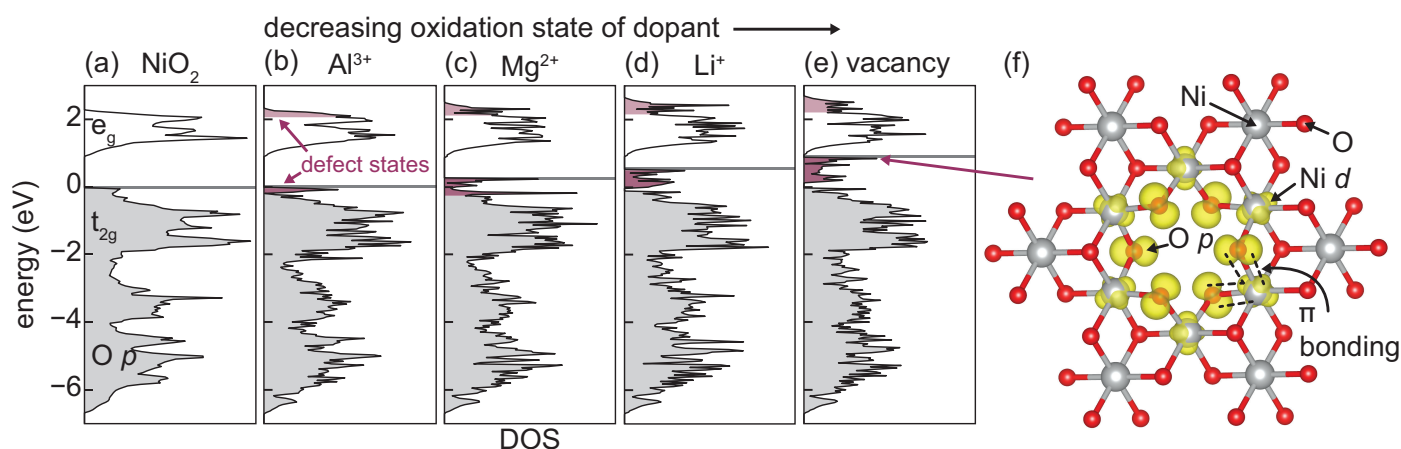


Fig. 5 DOS of $D_{1/16}\text{Ni}_{15/16}\text{O}_{32}$ for $D = \text{Ni}, \text{Al}, \text{Mg}, \text{Li},$ or vacancy ((a)-(e), respectively). The oxidation state of the dopant decreases from left to right and is compensated by a background electronic charge. Bands with majority contribution from O p and Ni d orbitals around the defect (i.e. defect states) are highlighted in red. Occupied defect states just below the Fermi level increase in energy with decreasing oxidation state of dopant. (f) Partial charge density of the highest occupied band looking down on a layer of $\text{Ni}_{1.5/16}\text{O}_{32}$. Large O p and Ni d orbitals are localized around the atoms near the vacancy and appear to be π bonding. (Images made using VESTA²⁸)

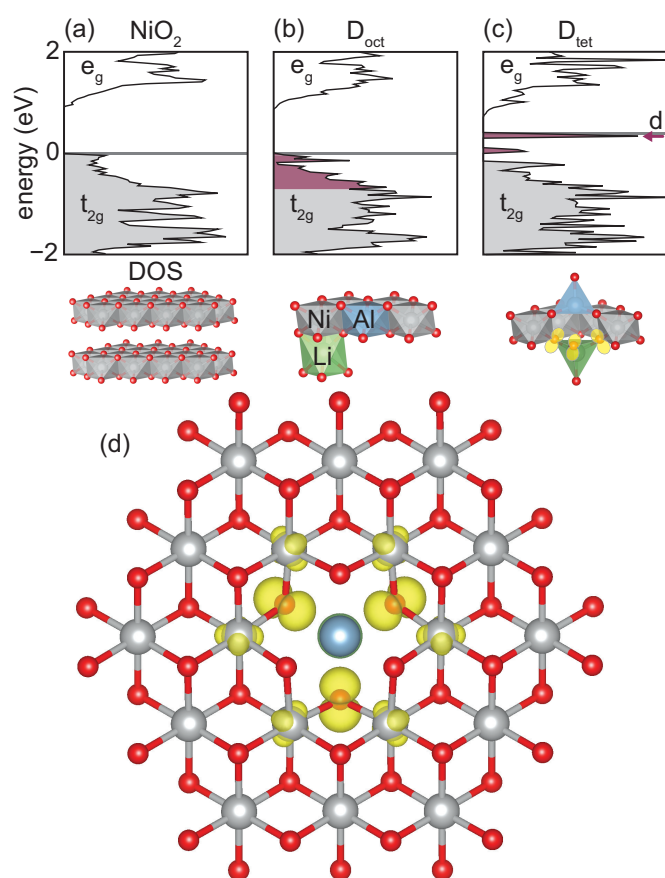


Fig. 6 DOS of (a) layered bulk NiO_2 , (b) octahedral Al dopant in the TM layer with Li for charge balance in the Ni host, and (c) Li-Al dumbbell in the Ni host. Defect states are highlighted in red. (d) The partial charge density of the highest occupied band of the D_{tet} configuration. The O p lobes in (d) are on the O next to Li, as indicated in yellow on the structure in (c). (Images made using VESTA²⁸)

bor the Al dopant. Not all O p states that point to the Al, however, contribute to the high energy defect states. Only those O that are not coordinated by a Li in the Li layer participate in the defect states. These O atoms are surrounded by less positive charge and therefore have a higher energy.

The Li-Al D_{tet} configuration produces defect states at even higher energies (Figure 6 (c)). The electronic charge density associated with the highest energy defect state is shown in Figure 6 (d). The defect state is again primarily composed of π bonded O p orbitals and Ni d orbitals. Only the O p orbitals that belong to the base of the tetrahedron occupied by Li and that point to the octahedral vacancy participate in bonding. These particular O p levels have a high energy as they are coordinated by the low positive charge of Li. The similar O p orbitals of the base of the tetrahedron occupied by Al are surrounded by substantially higher positive charge and therefore have a lower energy. The D_{tet} configuration results in a significant increase of the Fermi level since the defect states in the Ni host remain occupied. As shown in Figure 3, the D_{tet} configuration is 1.2 eV/dopant higher in energy than the D_{Oct} configuration. At room temperature, few dumbbells are therefore expected to form.

It is also instructive to consider the change in electronic structure when Li serves as a dopant in the TM layer as it has a much lower oxidation state. Four Li must be present in the structure for every TM that is removed to maintain charge neutrality in the fully charged state. The lowest energy D_{Oct} and D_{tet} configurations are ones that cluster Li around the defect, as illustrated in Figure 7(b) and (c). In the D_{Oct} configuration (Figure 7(b)), large spikes in DOS appear at the top of the occupied states, similar to ones seen for NiO_2 with a Li-Al dumbbell (Figure 6(c)). Similar high energy defect states appear in the Li-Li D_{tet} configuration (Figure 7(c)). The highest energy states for D_{tet} are associated with the O that have only one adjacent Li. The defect states that are slightly lower in energy derive from the O that are coordinated by two adjacent Li. This is shown in representative

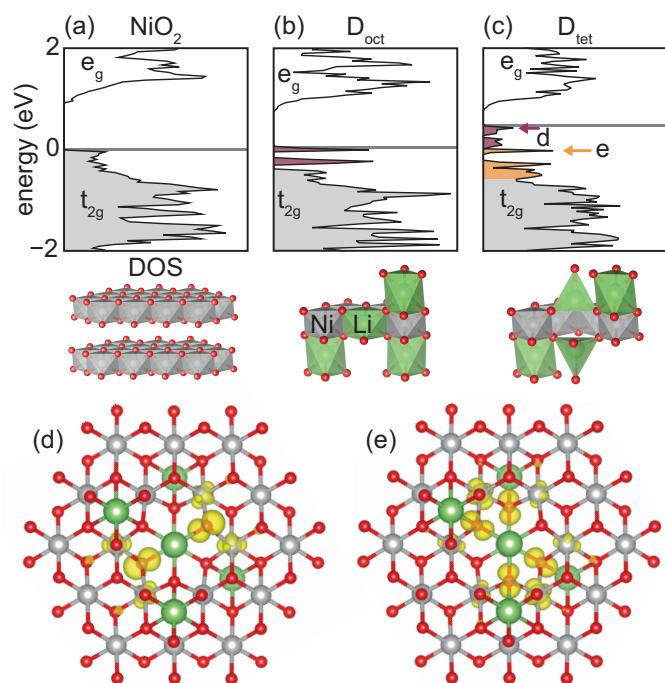


Fig. 7 DOS of (a) layered bulk NiO₂, (b) octahedral Li dopant in the Ni host, and (c) Li-Li dumbbell in the Ni host. (d) Partial charge density of a band at the top of the occupied bands with O *p* character on oxygen not adjacent to additional Li atoms, highlighted in red. (e) Partial charge density of a band slightly lower in energy with O *p* character on oxygen adjacent to an additional Li atom, highlighted in orange. (Images made using VESTA²⁸)

partial charge densities in Figures 7(d) and (e). While the Fermi level does increase when going from the D_{Oct} configuration to the D_{Tet} configuration, the overall energy of the D_{Tet} configuration is lower than D_{Oct} by 100 meV/dopant. Li-Li dumbbells are therefore favored upon delithiation.

The electronic structures of the Co and Mn hosts are very different from those just described for NiO₂. Both Co and Mn have fewer electrons than Ni and therefore CoO₂ and MnO₂ only partially fill their *t*_{2g} states. Furthermore, CoO₂ and MnO₂ exhibit a net magnetic moment when initialized in the ferromagnetic state (Figure 8(a) and (e)). The CoO₂ system exhibits a relatively weak exchange splitting, with the spin-up and spin-down DOS only slightly offset from each other. One of the spin channels has the *t*_{2g} states almost completely filled, while the other has more empty *t*_{2g} states. In MnO₂, the difference is more drastic; *t*_{2g} states of one of the spin channels fills completely while those of the other reside much higher in energy and therefore stay empty.

Figure 8 shows the DOS for an Al dopant in Co and Mn hosts. The defect states are more delocalized in the D_{Oct} configuration in these two hosts with the Al dopant than was the case in the Ni host and are therefore not easily distinguishable from the total DOS. The defect states are more pronounced in the D_{Tet} configurations (highlighted red in Figures 8(c) and (f)), exhibiting a significant increase in DOS at the top of the *t*_{2g} block. The distinction is based on O *p* pDOS (figure in ESI), where the defect states are characterized by a spike in density for O atoms surrounded

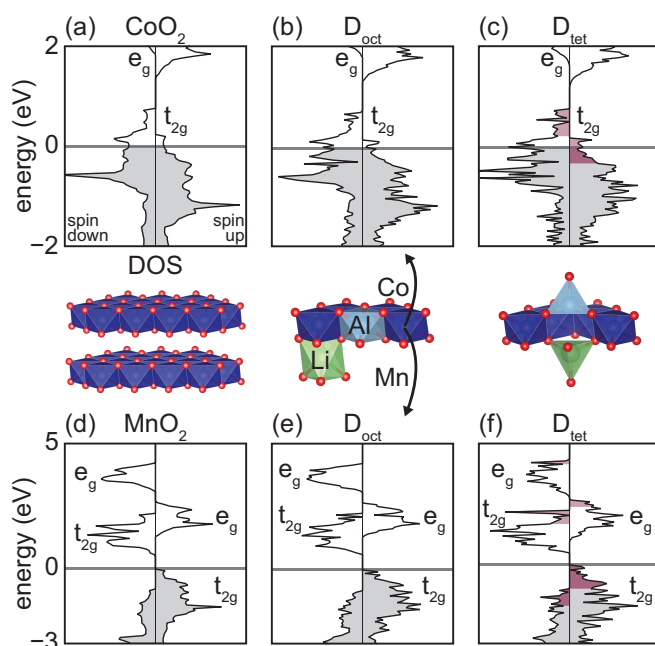


Fig. 8 DOS of (a) layered bulk Co, (b) octahedral Li-Al defect in the Co host, (c) dumbbell Li-Al defect in Co host, (d) layered bulk MnO₂, (e) octahedral Li-Al defect in the Mn host, and (f) dumbbell Li-Al defect in the Mn host. Defect states overlap strongly with the rest of the *t*_{2g} bands in the D_{Oct} configurations, but are highlighted in red for the D_{Tet} configurations. (Images made using VESTA²⁸)

by the least positive charge (in this case, adjacent to tetrahedral Li). Since the defect states reside at the top of the *t*_{2g} block in both spin channels, not all of them need to be filled in the Co and Mn hosts. The energetic penalty for forming the D_{Tet} relative to the D_{Oct} configuration is, therefore, much lower in the Co and Mn hosts since some of the defect states can remain empty. In the Mn host, the Li-Al D_{Oct} configuration is slightly more stable than the D_{Tet} configuration by 65 meV/defect while the two configurations are essentially degenerate in the Co host. This is in stark contrast to the highly unfavorable Li-Al dumbbell in the Ni host. Similarly, for the Li-Mg and Li-Li defects, the D_{Tet} configurations are favored more for Co and Mn hosts than for the Ni host.

With this new theoretical understanding, we return to the experimental results presented in Figure 1. As the defect states are completely occupied in the Ni host but only partially filled in the Co host, our calculations predict that more Li-Al dumbbells will form in the latter due to entropic factors. Figure 3 shows that there is essentially no energy difference between the D_{Oct} and D_{Tet} configurations in the Co host, but a sizable energy penalty for D_{Tet} in the Ni host. Since the synthesized particles of the different compositions had comparable surface areas, surface interactions with the electrolyte are unlikely to result in the stark difference in capacity loss behavior between Ni and Co hosts.²¹ Furthermore, Nuclear Magnetic Resonance (NMR) findings strongly support that Al does migrate into tetrahedral sites in the Co host and not in the Ni host.²¹ The experimental conditions should allow for interlayer atom migration because the cells are cycled to very high voltages (upwards of 4.75 V) and are thus able to ap-

proach the limits of delithiation. Only at high voltages, when the only remaining Li in the material is that pinned by the redox inactive dopant, can the Al migrate into the Li layer of the Co host. Our calculations indicate that Mg-doped Co, Ni, and Mn hosts may also show a large discrepancy in capacity loss between the hosts, but comparable experiments at high voltage have yet to be performed on Mg-doped Co and Ni hosts. These experiments are beyond the scope of this study.

6 Discussion

Layered transition metal oxide intercalation compounds remain the cathode material of choice in current Li-ion battery technologies. However, only 50-70 % of the theoretical capacity of these cathode materials is currently utilized due to the rapid degradation that occurs at high states of charge.⁴ Many layered intercalation compounds tend to become highly metastable upon the complete removal of Li ions and are susceptible to structural changes due to transition metal and dopant migration to the emptied Li layers.

In this study, we used electronic structure calculations to determine the effects of chemistry on the susceptibility of dopant migration in O3 layered transition-metal oxides. A dopant that migrates from the TM layer to the Li layer must first pass through an intermediate tetrahedral site. The most stable intermediate configuration is one in which the dopant forms a dumbbell with a residual Li. Our calculations have shown that the stability of Li-dopant dumbbells in the fully charged state is highly sensitive to the identity of TM cations surrounding the dopant site: a Ni host tends to suppress Li-dopant dumbbell formation while Co and Mn hosts favor their formation. This remarkable result suggests that targeted alloying of layered transition metal oxides can serve as an effective strategy to suppress dopant migration at high states of charge.

The stark difference in the susceptibility of dopants to migrate to the Li layer between the Ni host on the one hand and Co and Mn hosts on the other has its origin in electronic structure. Figure 9 schematically summarizes the essential features of the DOS of pure and doped transition metal oxides as distilled from the detailed electronic structure calculations of the previous sections. The electronic structure of the pure hosts, in the absence of dopants, consists of three major blocks: low energy states having predominantly O *p* character; *t*_{2g}-like states made up of π bonded transition metal *d* orbitals and O *p* orbitals; and anti-bonding *e*_g-like states. In NiO₂, the Fermi level resides between the *e*_g block and the *t*_{2g} block. In CoO₂ and MnO₂, in contrast, the Fermi level resides in the *t*_{2g} block. Some of the higher energy *t*_{2g}-like states that are made up of π bonded TM *d* orbitals and O *p* orbitals are empty in Co- and Mn-rich compounds.

The emergence of localized defect states and their high energy are closely linked to the fact that the dopant oxidation states are lower than 4+ and that they do not have *d* orbitals. A lower amount of coordinating positive charge lifts the energy of the O *p* orbitals near the defect such that they form localized states. This ionic interaction is illustrated by the rise in the energy of the defect states with the reduction in the oxidation state of an octahedral dopant in Figure 5. Hybridization between the O *p* and

TM *d* orbitals also plays a role in the origin of the defect states. The O *p* orbitals involved in the defect states just above the *t*_{2g} block are orbitals that in the pristine material would exhibit a σ interaction with the *d* orbitals of the missing TM, making them dangling bonds. Although such states are often referred to as orphaned states in the context of Li-excess materials,^{37,38} they nevertheless exhibit π bonds with the surrounding TM ions. This π interaction can be seen in Figures 5, 6, and 7, which show that the defect states have significant contributions not only from O but also from the remaining neighboring TM cations.

Since the defect states appear at the top of the *t*_{2g} block, the position of the Fermi level determines the extent to which they are occupied. In systems where the TM has sufficient electrons to fill all of the *t*_{2g} states, the defect states are completely filled and significantly contribute to the overall energy (Figures 9(a) and (b)). In systems with fewer electrons, where the Fermi level resides within the *t*_{2g} block, at least some of the defect states may remain empty, reducing their contribution to the overall energy (Figures 9(c) and (d)). Therefore, systems that do not fully fill the *t*_{2g} bands are less affected by dopant inclusion and have a smaller penalty for dumbbell formation.

In addition to TM identity, Figure 3 shows that the identity of the migrating species has a strong effect on the stability of the D_{tet} configurations. Dopants with a lower oxidation state, like Li, are more likely to form dumbbells than cations like Al, which has a higher oxidation state. Cation size alone cannot explain this trend as Li and Mg both have very similar sizes, but Li has lower dumbbell formation energies in all three hosts. Instead, there is likely a smaller penalty from the defect states for D_{tet} configurations when the dopant has a lower oxidation state. Dumbbell formation energy is the difference in energy between the D_{Oct} and D_{tet} configurations. This energy is high for dopants like Al because the difference between the electrostatic potential for certain O atoms changes drastically when the Al moves from the TM layer into the tetrahedral site. However, the local environment around the O is similar for D_{Oct} and D_{tet} when Li is the dopant. The defect states are already very high in energy when the Li is in the TM layer, as evidenced by the DOS in Figure 7(b), so that a change to the tetrahedral site does not raise the energy of the defect states.

We completed additional calculations to confirm that differences in the lattice parameters of the hosts were not responsible for the difference in dumbbell formation energies. We performed static calculations of the D_{Oct} and D_{tet} configurations using the relaxed lattice parameters of the other two hosts (e.g. we imposed the Ni and Co host lattice parameters on the Mn host and vice versa) to determine if the particular lattice parameters were responsible for the trend in dumbbell formation energies (details and results in the ESI). Even when the lattice parameters of the Co or Mn hosts were imposed on LiAlNi₁₅O₃₂, the dumbbell formation energy was around 1 eV/Al. Alternatively, the Ni host lattice parameters did not make the dumbbell significantly less stable in LiAlCo₁₅O₃₂ and LiAlMn₁₅O₃₂. We also found that when the atomic positions were kept constant, Li was still more likely to form dumbbells than Al. Therefore, the qualitative dumbbell formation trends seen in Figure 3 cannot be ascribed to size ef-

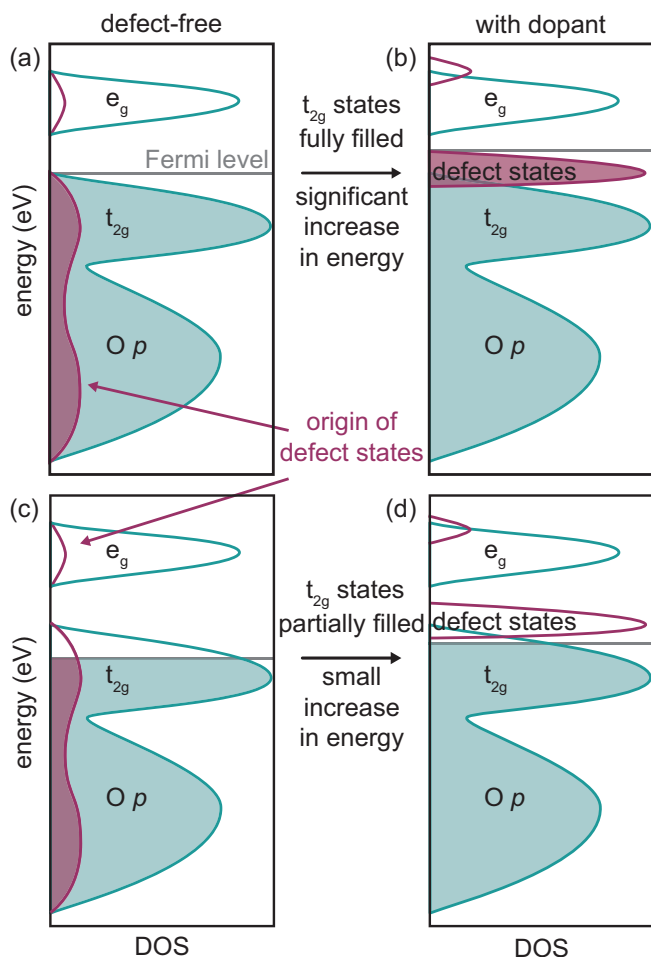


Fig. 9 Schematic representation of DOS for defect-free and doped layered oxides. (a) Defect-free layered oxide with all t_{2g} states filled, as in NiO_2 and (b) that layered oxide doped with a lower oxidation-state ion, such as Al in the Ni host. Defect states increase the overall energy of the system. (c) Defect-free layered oxide where the TM has fewer electrons, for instance CoO_2 , and (d) that layered oxide doped with a lower oxidation state ion, for instance Al in the Co host. The high-energy defect states do not have to be filled, so the energy increases less than for the case above.

facts.

The trends described so far are not restricted to dopant migration. They also apply to transition metal migration. We performed calculations to determine the change in energy when a Ni or Co atom migrates from the TM layer to an adjacent tetrahedral site of an empty Li layer in both a Ni and Co host. The barriers are lower bounds in the fully charged state when all of the transition metals are in a formal 4+ oxidation state. The tetrahedral defect formation energies were predicted to be 2.75 and 2.61 eV/defect for a Ni and Co in the Ni host, respectively, while they were 1.34 and 1.29 eV/defect for Ni and Co in the Co host, respectively. All four energies are high and positive, indicating a high kinetic barrier for TM migration to the empty Li layers of fully charged Co or Ni hosts. Similar to the dopant dumbbell formation energies, however, the calculated energies only marginally depend on the identity of the migrating cation, but instead depend strongly on the host chemistry. The barrier for TM migration to empty Li layers is substantially higher in the Ni host than in the Co host, differing by over 1eV. We emphasize that these trends are predicted for the fully delithiated Ni host. It is well known that Li_xNiO_2 usually contains a small percentage of Ni in the Li layer.^{13,39} However, these extra Ni are introduced during high temperature synthesis in the fully lithiated state.

All first-principles results reported in this study were based on density functional theory using a PBE functional as described in the Calculation Methods section. It is generally accepted that a DFT+ U approach^{40,41} is necessary to accurately describe the electronic structure of TM oxides.⁴² Here we found that the predictions are both qualitatively and in large part quantitatively insensitive to approximations to DFT. Values of + U corrections ranging between 0 and 5 were used to calculate the energies of Li-Al D_{Oct} and D_{Tet} configurations in Ni and Mn hosts (use of + U in Co oxides has been shown to result in incorrect ground state configurations^{43,44}). Dumbbell formation energies and the qualitative shape of the DOS were very similar for all values of the Hubbard U (see figures in SI). The invariance of the predicted energy differences to the value of + U is likely due to the fact that all transition metals are in their 4+ oxidation state and remain in that state for each dopant configuration.

The correlations revealed in this study between electronic structure and the susceptibility for interlayer migration in TM oxides can be utilized in cathode design. Alloying strategies that maximize the filling of the t_{2g} states, and therefore all localized defect states, when the battery is fully charged will penalize dumbbell formation and hence cation migration to the Li layer. In general, an increase in the Ni concentration can be a simple solution for systems where dumbbell formation must be suppressed to improve kinetics and cycleability. The favorable cycling behavior of Ni-rich NCA compounds ($\text{Li}_x(\text{Ni}_{1-y-z}\text{Co}_y\text{Al}_z)\text{O}_2$) is consistent with the predictions of this work.²¹ Our study suggests that dopant migration is likely to contribute significantly to cathode degradation at high states of charge in Co-rich chemistries. Mg, for example, is used as a dopant in Li_xCoO_2 to suppress the two-phase region between $x = 0.93$ and 0.75.²² The predictions of this study indicate that Mg dopants will experience a driving force to migrate to the Li layer in the fully charged state, thereby caus-

ing irreversible changes to the host crystal structure. An increase in the Ni content will suppress these tendencies, while the addition of Mn will not. Of course, other factors will also need to be taken into consideration when varying transition metal chemistry, including the effect of such variations on the intrinsic electronic conductivity of the compound.

The results presented here also suggest that certain dopants could promote the degradation of the cathode through oxygen evolution. In cases where defect states are unoccupied (such as the Li-Al dumbbell in the Co host), the O *p* states near the defect are significantly depleted. Prior calculations suggest that this depletion of O *p* states could enable the dimerization of oxygen and subsequent formation of O₂ molecules, leading to irreversible degradation of the material.⁴⁵ This suggests that the tetrahedral migration of dopants may negatively impact the reversibility of electrodes not only by causing a redistribution of cations but also by triggering oxygen loss.

Lastly, while the experimental cycling results shown in Figure 1 correlate well with conclusions from our computational work, more direct observations of dopant migration would enhance our understanding of this mechanism. NMR measurements have already indicated the presence of Al in the Li layer of Co rich hosts but not in the Ni rich hosts.²¹ Though the positions of disordered dopants can be difficult to characterize with common methods such as X-ray diffraction (XRD), other spectroscopic techniques including X-ray absorption spectroscopy (XAS) and resonant inelastic X-ray scattering (RIXS) could be used to characterize differences in electronic structure between Al doped Ni-rich and Co-rich hosts.^{46,47} Signatures of the electronic defect states will provide information as to whether or not dumbbells form. It is important, however, to recognize that any ex situ probes have their limitations as these materials are highly metastable at high states of charge and may readily decompose upon removal from the battery.⁴

7 Conclusions

Irreversible structural changes in the cathode at the end of charge are a significant hurdle that inhibits further capacity utilization in current battery materials. In order to surmount this challenge, a better understanding of cation migration as a function of cathode composition is critical. Using first-principles calculations, we have demonstrated a strong correlation between the identity of the transition metal and the energy barrier for cation migration to empty Li layers of fully charged layered intercalation compounds. We show that oxides with higher concentrations of Co or Mn are likely to experience enhanced rates of interlayer atom migration, while an increase in the Ni concentration should suppress migration and stabilize the layered structure at high states of charge. The origins of this sensitivity to chemistry are rooted in electronic structure. We speculate that the behavior in battery materials having other crystal structures or utilizing different intercalants leads to similar electronic structure effects. The implications of our work can be extended to better understand oxygen dimerization and gas evolution, which is also detrimental for battery performance. Considering that interlayer migration can result in irreversible capacity loss, these new insights suggest a clear path

to the discovery of cathode chemistries that can achieve practical capacities approaching their theoretical values.

8 Methods

8.1 Experimental

LiAl_yNi_{1-y}O₂ and LiAl_yCo_{1-y}O₂ (0 ≤ *y* ≤ 0.2) materials were synthesized as described in Ref 21. Stoichiometric amounts of lithium acetate, aluminum acetate basic hydrate, nickel(II) acetate tetrahydrate, and cobalt(II) acetate were mixed in deionized water, dried, and annealed to create the active materials. Free-standing positive electrodes using LiAl_yNi_{1-y}O₂ and LiAl_yCo_{1-y}O₂ active materials were fabricated in the dry room using the Bellcore method.⁴⁸ The casting slurries were comprised of a mixture of the active material, poly(vinylidene fluoride-co-hexafluoropropylene) (PVDF-HFP, Kynar 2801, Elf Atochem), carbon black (Super P (SP), MMM), propylene carbonate (≥ 99.7%, Aldrich), and acetone (≥ 99.7%, Aldrich). The slurries were mixed until homogeneous, then cast and allowed to air dry. The propylene carbonate plasticizer was removed by soaking the electrode in anhydrous diethyl ether (99.8%, Aldrich). Electrodes were subsequently dried at 120 °C under vacuum for a minimum of 10 hours, and stored in an Ar-atmosphere glovebox to avoid atmospheric exposure. The resulting self-standing electrodes each had a composition of 79.9 wt.% active material, 7.0 wt.% SP, and 13.1 wt.% PVDF-HFP. The fraction of conductive carbon black is higher than that of commercial cells, resulting in a lower loading of active material. This ratio was deliberately chosen to isolate the effect of Al concentration on irreversible loss, independent of the intrinsic transport capabilities (either good or bad) of the active material. The experimental studies were not designed to probe transport properties of the electrodes.

Metal mixing over the TM sites of the layered materials was confirmed with transmission electron microscopy (TEM) and nanometer resolution X-ray energy dispersive spectroscopy (EDS).²¹ Except for LiAl_{0.2}Ni_{0.8}O₂, the composition of which is very close to the phase segregation limit, all materials had well-mixed transition metals. Since changes in synthesis can have a significant effect on battery performance, care was taken to ensure consistent preparation of the materials. Commercially available LiCoO₂ was used as a model for comparison and showed good X-ray diffraction (XRD) correspondence to its in-house synthesized counterpart.

Coin cells with Al-clad positive bases (2032, Hohsen Corp.) were assembled in an Ar-filled glovebox (< 0.1 ppm of H₂O and O₂) using a Li metal (FMC Lithium) negative electrode and Whatman GF/D glass fiber separators saturated with a 1M LiPF₆ ethylene carbonate: dimethyl carbonate (EC:DMC) (1:1 volume ratio) electrolyte (BASF) (< 20 ppm H₂O). Electrochemical characterization was performed with a VMP3 (Bio-Logic Science Instruments) at 24 °C. Cells were galvanostatically charged at 20 mA/g (per g of active material) to 4.75 V, held under potentiostatic conditions until the current dropped below 10 mA/g, and then discharged at 10 mA/g to 2.75 V. The hold time at the fully charged state varied slightly as the cells were charged at 20 mA/g and held at high voltage until current dissipated to 10 mA/g. As

such, hold times were dependent on the kinetics of the materials; the typical time was less than 0.5 h. Duplicate cells were made to ensure reproducibility.

8.2 Computational

Density functional theory (DFT) was utilized to calculate energies and electronic band structures using the Vienna Ab Initio Simulation Package (VASP)^{49,50} with the PAW method^{51,52} and the optb86b-vdw functional.^{53–56}

First, a 4×4 unit cell of NiO_2 was generated and one of the Ni atoms was replaced by a dopant, resulting in the formula $X_{1/16}\text{Ni}_{15/16}\text{O}_{32}$, where $X = \text{Al}, \text{Mg}, \text{Li}$, or vacancy. Electrons were artificially added to the system to enable a formal oxidation state of $4+$ for all Ni, while the dopants could remain in their preferred formal oxidation states of Al^{3+} , Mg^{2+} , Li^+ , or Va^0 .

Second, 4×4 unit cells of MO_2 ($M = \text{Co}, \text{Mn}$, or Ni) were generated. In each case, one of the TM atoms was replaced by a Li, Mg, or Al dopant. In addition, Li was added to the structures, with resulting compositions $\text{LiAlM}_{15}\text{O}_{32}$, $\text{Li}_2\text{MgM}_{15}\text{O}_{32}$, and $\text{Li}_4\text{M}_{15}\text{O}_{32}$ ($M = \text{Co}, \text{Mn}$, or Ni). In addition to keeping the dopant in the TM layer, another set of similar cells was generated in which the dopant was moved to an adjacent tetrahedral site in the Li layer, leaving behind a vacancy in the TM layer. In both cases, many configurations were sampled using the CASM software^{57–60} and lowest energy configurations were used for determining dumbbell formation energy.

More details on the computational methods are provided in the ESI. In addition, data files are publicly available at [link provided before publication].

Conflicts of Interest

There are no conflicts to declare.

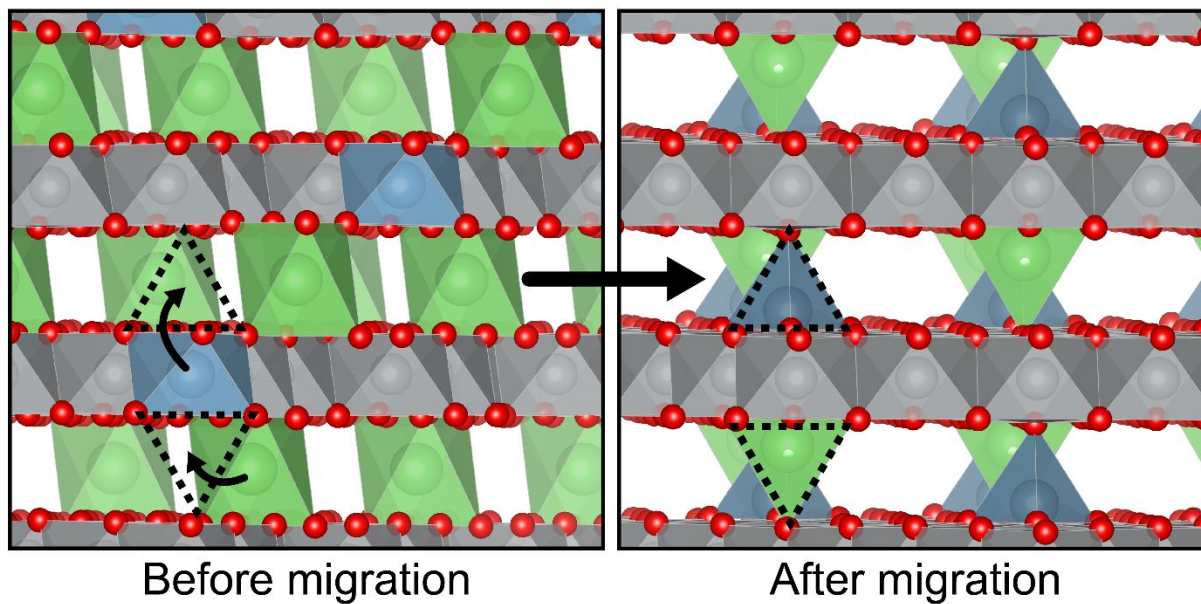
Acknowledgments

This material is based upon work supported by the National Science Foundation, Grant DMR-1410242. We acknowledge support from the Center for Scientific Computing from the CNSI, MRL, NSF MRSEC (DMR-1121053), and Hewlett-Packard. This research used resources of the National Energy Research Scientific Computing Center, a DOE Office of Science User Facility supported by the Office of Science of the U.S. Department of Energy under Contract No. DE-AC02-05CH11231. This material is also based upon work supported as part of the NorthEast Center for Chemical Energy Storage (NECCES), an Energy Frontier Research Center funded by the U.S. Department of Energy, Office of Science, Office of Basic Energy Sciences under Award Number DE-SC0012583.

Notes and references

- 1 K. Mizushima, P. C. Jones, P. J. Wiseman and J. B. Goodenough, *Mat. Res. Bull.*, 1980, **15**, 783–789.
- 2 M. Thackeray, C. Wolverton and E. Isaacs, *Energy Environ. Sci.*, 2012, **5**, 7854–7863.
- 3 N. Nitta, F. Wu, J. T. Lee and G. Yushin, *Mater. Today*, 2015, **18**, 252–264.
- 4 M. D. Radin, S. Hy, M. Sina, C. Fang, H. Liu, J. Vinckeviciute, M. Zhang, M. S. Whittingham, Y. S. Meng and A. Van der Ven, *Adv. Energy Mater.*, 2017, **7**, 1602888(1–33).
- 5 F. Schipper, E. M. Erickson, C. Erk, J.-Y. Shin, F. F. Chesneau and D. Aurbach, *J. Electrochem. Soc.*, 2017, **164**, A6220–A6228.
- 6 S. Hy, H. Liu, M. Zhang, D. Qian, B.-J. Hwang and Y. S. Meng, *Energy Environ. Sci.*, 2016, **9**, 1931–1954.
- 7 *Energy Environ. Sci.*, 2018, **11**, 1470–1479.
- 8 H. Liu, H. Liu, I. D. Seymour, N. Chernova, K. M. Wiaderek, N. M. Trease, S. Hy, Y. Chen, K. An, M. Zhang, O. J. Borkiewicz, S. H. Lapidus, B. Qiu, Y. Xia, Z. Liu, P. J. Chupas, K. W. Chapman, M. S. Whittingham, C. P. Grey and Y. S. Meng, *J. Mater. Chem. A*, 2018, **6**, 4189–4198.
- 9 T. Ohzuku, A. Ueda and M. Kouguchi, *J. Electrochem. Soc.*, 1995, **142**, 4033–4039.
- 10 T. Ohzuku, T. Yanagawa, M. Kouguchi and A. Ueda, *J. Power Sources*, 1997, **68**, 131–134.
- 11 S. Madhavi, G. V. Subba Rao, B. V. R. Chowdari and S. F. Y. Li, *J. Power Sources*, 2001, **93**, 156–162.
- 12 C. Vogler, B. Löffler, W. Weirather, M. Wohlfahrt-Mehrens and J. Garche, *Ionics*, 2002, **8**, 92–99.
- 13 C. Delmas, M. Ménétrier, L. Croguennec, I. Saadoune, A. Rougier, C. Pouillier, G. Prado, M. Grüne and L. Fournès, *Electrochim. Acta*, 1999, **45**, 243–253.
- 14 C. Pouillier, L. Croguennec, P. Biensan, P. Willmann and C. Delmas, *J. Electrochem. Soc.*, 2000, **147**, 2061–2069.
- 15 C.-C. Chang, J. Y. Kim and P. N. Kumta, *J. Electrochem. Soc.*, 2000, **147**, 1722–1729.
- 16 T. Sasaki, V. Godbole, Y. Takeuchi, Y. Ukyo and P. Novak, *J. Electrochem. Soc.*, 2011, **158**, A1214–A1219.
- 17 G. G. Amatucci, J. M. Tarascon and L. C. Klein, *J. Electrochem. Soc.*, 1996, **143**, 1114–1123.
- 18 A. Van der Ven, M. K. Aydinol, G. Ceder, G. Kresse and J. Hafner, *Phys. Rev. B*, 1998, **58**, 2975–2987.
- 19 A. Van der Ven, M. K. Aydinol and G. Ceder, *J. Electrochem. Soc.*, 1998, **145**, 2149–2155.
- 20 Z. Chen, Z. Lu and J. R. Dahn, *J. Electrochem. Soc.*, 2002, **149**, A1604–A1609.
- 21 N. V. Faenza, N. Pereira, D. M. Halat, J. Vinckeviciute, L. Bruce, M. D. Radin, P. Mukherjee, F. Badway, A. Halajko, F. Cosanday, C. P. Grey, A. Van der Ven and G. G. Amatucci, *Chem. Mater.*, 2018, **30**, 7545–7574.
- 22 H. Tukamoto and A. R. West, *J. Electrochem. Soc.*, 1997, **144**, 3164–3168.
- 23 C. P. Grey, W.-S. Yoon, J. Reed and G. Ceder, *Electrochem. Solid-State Lett.*, 2004, **7**, A290–A293.
- 24 M. S. Islam, D. J. Driscoll, C. A. Fisher and P. R. Slater, *Chem. Mater.*, 2005, **17**, 5085–5092.
- 25 R. Amin and J. Maier, *Solid State Ion.*, 2008, **178**, 1831–1836.
- 26 J. Chen and J. Graetz, *ACS Appl. Mater. Inter.*, 2011, **3**, 1380–1384.
- 27 R. Malik, D. Burch, M. Bazant and G. Ceder, *Nano Lett.*, 2010, **10**, 4123–4127.

- 28 K. Momma and F. Izumi, *J. Appl. Crystallogr.*, 2011, **44**, 1272–1276.
- 29 M. S. Islam and C. A. J. Fisher, *Chem. Soc. Rev.*, 2014, **43**, 185–204.
- 30 Z. Rong, R. Malik, P. Canepa, G. Sai Gautam, M. Liu, A. Jain, K. Persson and G. Ceder, *Chem. Mater.*, 2015, **27**, 6016–6021.
- 31 J. Bhattacharya and A. Van der Ven, *Phys. Rev. B*, 2011, **83**, 144302(1–9).
- 32 A. Van der Ven, J. Bhattacharya and A. A. Belak, *Acc. Chem. Res.*, 2013, **46**, 1216–1225.
- 33 A. Emly and A. Van der Ven, *Inorg. Chem.*, 2015, **54**, 4394–4402.
- 34 A. Van der Ven and G. Ceder, *Electrochem. Commun.*, 2004, **6**, 1045–1050.
- 35 J. Reed, G. Ceder and A. Van Der Ven, *Electrochem. Solid-State Lett.*, 2001, **4**, A78–A81.
- 36 J. Reed and G. Ceder, *Chem. Rev.*, 2004, **104**, 4513–4534.
- 37 D.-H. Seo, J. Lee, A. Urban, R. Malik, S. Kang and G. Ceder, *Nat. Chem.*, 2016, **8**, 692–697.
- 38 G. Assat and J.-M. Tarascon, *Nat. Energy*, 2018, **3**, 373–386.
- 39 C. Delmas, J. Pérès, A. Rougier, A. Demourgues, F. Weill, A. Chadwick, M. Broussely, F. Pertont, P. Biensan and P. Willmann, *J. Power Sources*, 1997, **68**, 120–125.
- 40 V. I. Anisimov, F. Aryasetiawan and A. I. Lichtenstein, *J. Phys.: Condens. Matter*, 1997, **9**, 767–808.
- 41 S. L. Dudarev, G. A. Botton, S. Y. Savrasov, C. J. Humphreys and A. P. Sutton, *Phys. Rev. B: Condens. Matter Mater. Phys.*, 1998, **57**, 1505–1509.
- 42 F. Zhou, M. Cococcioni, C. A. Marianetti, D. Morgan and G. Ceder, *Phys. Rev. B*, 2004, **70**, 235121(1–8).
- 43 Y. S. Meng, Y. Hinuma and G. Ceder, *J. Chem. Phys.*, 2008, **128**, 104708(1–8).
- 44 E. B. Isaacs and C. A. Marianetti, *Phys. Rev. B*, 2017, **95**, 045141(1–18).
- 45 H. Chen and M. S. Islam, *Chem. Mater.*, 2016, **28**, 6656–6663.
- 46 K. Luo, M. R. Roberts, R. Hao, N. Guerrini, D. M. Pickup, Y.-S. Liu, K. Edström, J. Guo, A. V. Chadwick, L. C. Duda and P. G. Bruce, *Nat. Chem.*, 2016, **8**, 684–691.
- 47 Z. Zhuo, C. D. Pemmaraju, J. Vinson, C. Jia, B. Moritz, I. Lee, S. Sallies, Q. Li, J. Wu, K. Dai, Y. D. Chuang, Z. Hussain, F. Pan, T. P. Devereaux and W. Yang, *J. Phys. Chem. Lett.*, 2018, **9**, 6378–6384.
- 48 J.-M. Tarascon, A. S. Gozdz, C. Schmutz, F. Shokoohi and P. C. Warren, *Solid State Ion.*, 1996, **86–88**, 49–54.
- 49 G. Kresse and J. Furthmüller, *Phys. Rev. B*, 1996, **54**, 11169–11186.
- 50 G. Kresse and J. Furthmüller, *Comput. Mater. Sci.*, 1996, **6**, 15–50.
- 51 G. Kresse and J. Hafner, *J. Phys.: Condens. Matter*, 1994, **6**, 8245–8257.
- 52 G. Kresse and D. Joubert, *Phys. Rev. B*, 1999, **59**, 1758–1775.
- 53 J. Klimeš, D. R. Bowler and A. Michaelides, *J. Phys.: Condens. Matter*, 2010, **22**, 074203(1–12).
- 54 M. Dion, H. Rydberg, E. Schröder, D. C. Langreth and B. I. Lundqvist, *Phys. Rev. Lett.*, 2004, **92**, 246401(1–4).
- 55 G. Román-Pérez and J. M. Soler, *Phys. Rev. Lett.*, 2009, **103**, 096102(1–4).
- 56 J. Klimeš, D. R. Bowler and A. Michaelides, *Phys. Rev. B: Condens. Matter Mater. Phys.*, 2011, **83**, 195131(1–13).
- 57 CASM, <https://github.com/prisms-center/CASMcode>.
- 58 J. C. Thomas and A. Van der Ven, *Phys. Rev. B: Condens. Matter Mater. Phys.*, 2013, **88**, 214111(1–13).
- 59 B. Puchala and A. Van der Ven, *Phys. Rev. B*, 2013, **88**, 094108(1–15).
- 60 A. Van der Ven, J. C. Thomas, Q. Xu and J. Bhattacharya, *Mathematics and Computers in Simulation*, 2010, **80**, 1393–1410.



Interlayer cation migration in layered cathodes, which can lead to irreversible capacity loss, is affected by surrounding transition metals.